



# Multi-dimensional modeling of large-scale lithium-ion batteries



Seunghun Jung\*, Dalmo Kang<sup>1</sup>

Battery R&D, LG Chem Research Park, 104-1, Moonji-dong, Yuseong-gu, Daejeon 305-380, Republic of Korea

## HIGHLIGHTS

- A noble multi-D mathematical model of large-scale lithium-ion batteries is developed.
- The model predicts current, voltage, temperature, SOC, and SOH distribution.
- The model performs simulation under dynamic operating conditions.
- Various experimental validations confirm that the model has high accuracy.

## ARTICLE INFO

### Article history:

Received 7 July 2013

Received in revised form

20 September 2013

Accepted 24 September 2013

Available online 5 October 2013

### Keywords:

Multi-dimension

Lithium-ion

Battery

Modeling

## ABSTRACT

Multi-dimensional model of large-scale lithium-ion batteries is developed. The model is based on equivalent circuit model (ECM) which is capable of dynamic response simulation. Model parameters are functions of both state of charge and temperature, which are implemented by bilinear interpolation method. Local degradation effects such as capacity fade and resistance growth are incorporated into the multi-D model by empirical method. Local distributions of current, potential, temperature, state of charge (SOC), and state of health (SOH) are observed with the developed model. It is found that local degradation worsens under severe operating condition. Low thermal conductivity of a battery results in non-uniform SOH distribution. Simulation result shows good agreement with experiment data under various operation modes.

© 2013 Elsevier B.V. All rights reserved.

## 1. Introduction

Since General Motors successfully launched the first plug-in hybrid electric vehicle (PHEV) powered by LG Chem's lithium-ion battery, lithium-ion battery has been getting more public interest as a strong candidate for future automotive power source. Compared to small batteries used for portable electronics which usually operate under steady, mild operating conditions, automotive batteries are exposed to more severe operating conditions. In addition, automotive batteries must sustain at least ten years with guarantee. For these reasons, it requires much time and efforts to develop lithium-ion batteries for automotive applications.

Mathematical modeling approach can be applied to battery engineering to save time and cost required for battery development. By solving governing equations, physics-based model [1–3]

can predict battery performance and analyze physical behavior before the actual battery is constructed. When a battery exists and experimental data of the battery is available, empirical models which mimic the battery performance can be generated. Equivalent circuit models [4–7] and fitting function models [8,9] belong to this category. As empirical models are relatively simple and fast, they are usually used as control algorithms for battery management system.

When the size of the battery becomes large, it is important to consider dimensional effects such as battery shape and lead-tab, or the high voltage outlet position on local distribution of current density, electrical potential, state of charge, and state of health. Most of mathematical models listed above are one-dimensional or lumped-scale models which are inadequate for analyzing dimensional affects. Therefore, it is necessary to apply multi-D modeling to design large-scale batteries. In development of an automotive battery pack which is usually cooled by liquid coolant or air-flow, computational fluid dynamics (CFD) is used to check thermal-fluidic behavior of the battery pack under various operating conditions. In order to accurately predict thermal-fluidic behavior of

\* Corresponding author. Tel.: +82 42 866 2094; fax: +82 42 862 1981.

E-mail addresses: [stratus76@hotmail.com](mailto:stratus76@hotmail.com) (S. Jung), [dalmo@lgchem.com](mailto:dalmo@lgchem.com) (D. Kang).

<sup>1</sup> Tel.: +82 42 870 6571; fax: +82 42 862 1981.

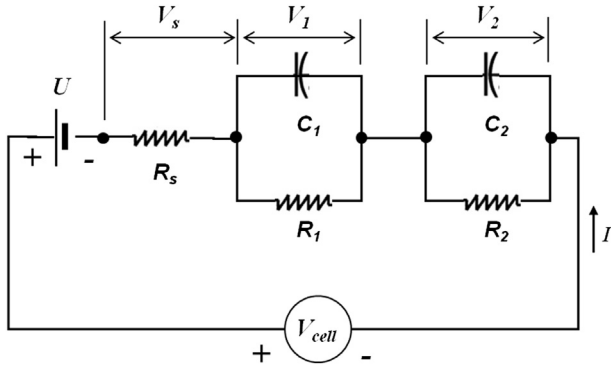


**Fig. 1.** Schematic of ECM with two RC-pairs representing a lithium-ion cell used for the present study.

the battery pack under given load condition, it is important to know the amount of heat generation which is directly affected by dynamic battery voltage. This battery voltage can be obtained by using multi-D battery model incorporated with CFD. Kwon et al. [8] extended Gu [9]'s circuit network based Zn/NiOOH cell model to two-dimensional lithium-ion cell model by solving positive and negative potential field instead of circuit network. This kind of model is typically called 'NTGK (Newman-Tiedemann-Gu-Kim) model'. NTGK model solves two electric potential fields coupled by fitting parameters acquired from constant discharging profile of a cell. This model is useful for predicting local distribution of electrical potential, temperature and SOC which come as dimensional effects in a large size battery. However, as the fitting parameters are functions of DOD (depth of discharge) and they do not have any time-dependent, relaxation terms. For this reason, NTGK model has limitation in simulating dynamic response to transiently changing load profile.

Mathematical battery models can be applied to battery life prediction also. Life prediction can be dealt with a physics-based approach which requires a deep understanding of degradation mechanism taking place in a lithium battery. Actually, this degradation mechanism is quite complex to explain with physics-based governing equation yet. Instead, a long-term battery life is typically estimated with empirical methods [10,11]. As a large-scale battery may have non-uniform degradation according to battery geometry, material properties, and operating condition, multi-D battery model can be useful to predict local degradation.

In this paper, we introduce how to develop an efficient multi-D battery model which can be applied to various purposes in the development of large-scale batteries.

## 2. Models

### 2.1. Equivalent circuit model

Equivalent circuit model (ECM) expresses a cell with simplified electric circuit. Fig. 1 shows a schematic of ECM with one serial resistance and two RC pairs (five ECM parameters total), which is used as a baseline mode for the present study. Cell voltage can be calculated by subtracting voltage losses from open circuit voltage ( $U$ ) which is a function of SOC as shown in Fig. 2.

$$V_{\text{cell}} = U - V_s - V_1 - V_2 \quad \text{where} \quad \begin{cases} U = f(\text{soc}) \\ \text{soc} = \text{soc}_0 - \frac{1}{\text{cap}_{\text{cell}}} \cdot \int_{\text{time}} I(t) \cdot dt \end{cases} \quad (1)$$

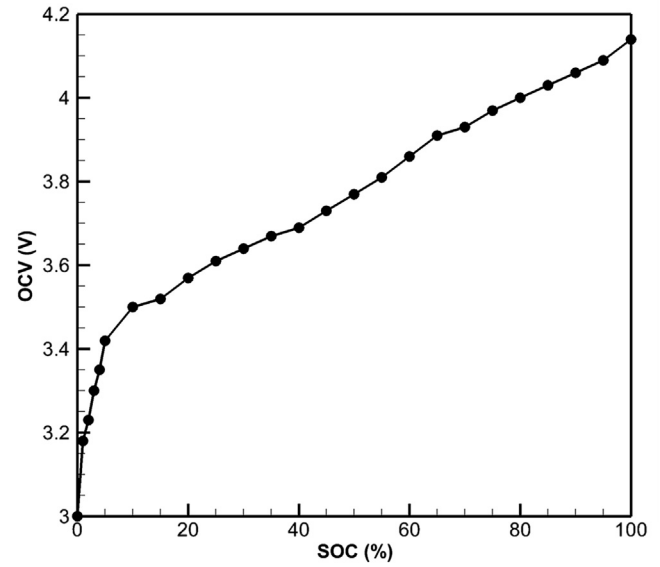


**Fig. 2.** OCV profile of the lithium-ion cell used for the present study.

From Kirchhoff's law, three voltage loss terms ( $V_s, V_1, V_2$ ) can be found as follows:

$$\begin{aligned} V_s &= I \cdot R_s \\ \frac{V_1}{R_1} + C_1 \frac{dV_1}{dt} &= I \\ \frac{V_2}{R_2} + C_2 \frac{dV_2}{dt} &= I \end{aligned} \quad (2)$$

Note that  $V_s$  is a function of only resistance ( $R_s$ ) whereas  $V_1$  and  $V_2$  are functions of both resistance and capacitance which has voltage relaxation effect during dynamic operation of a battery. Electric current,  $I$  is a function of time, not a constant here.

It is assumed that the serial resistance,  $R_s$  is a function of temperature while the RC-pair parameters ( $R_1, R_2, C_1, C_2$ ) are functions of both temperature and SOC. In order to minimize bias from temperature rise during experiment, ECM parameters are acquired from current-pulse and relaxation test (see Fig. 3) in this study. Iteratively comparing simulation result against experiment data, the model parameter for a given operating condition is found as an optimal fit. However, input variables such as SOC and temperature used for a model parameter continuously change when a cell operates. Therefore, model parameters should be updated at each time step by interpolation. In order to fit two-dimensional parameters such as RC-pairs that are functions of both temperature and SOC, a bilinear interpolation method is used as follows:

Table 1 is a two-dimensional experimental data of interested parameter such as  $y = R_1(T, \text{soc})$ . This experiment table must be filled out before starting interpolation. Four available temperature ( $-7^\circ\text{C}$ ,  $0^\circ\text{C}$ ,  $25^\circ\text{C}$ ,  $45^\circ\text{C}$ ) cases are used to build the model parameters for the present study. In order to find out value  $y$  at point ( $T, \text{soc}$ ) where experiment data does not exit, first, read value  $y$  of four neighboring points.

$$\begin{aligned} y_{11} &= R_1(T_1, \text{soc}_1) \\ y_{12} &= R_1(T_1, \text{soc}_2) \\ y_{21} &= R_1(T_2, \text{soc}_1) \\ y_{22} &= R_1(T_2, \text{soc}_2) \end{aligned} \quad (3)$$

Then, linear variable  $p$  and  $q$  are calculated as follows:

$$p = \frac{T - T_1}{T_2 - T_1}, \quad q = \frac{\text{soc} - \text{soc}_1}{\text{soc}_2 - \text{soc}_1} \quad (4)$$

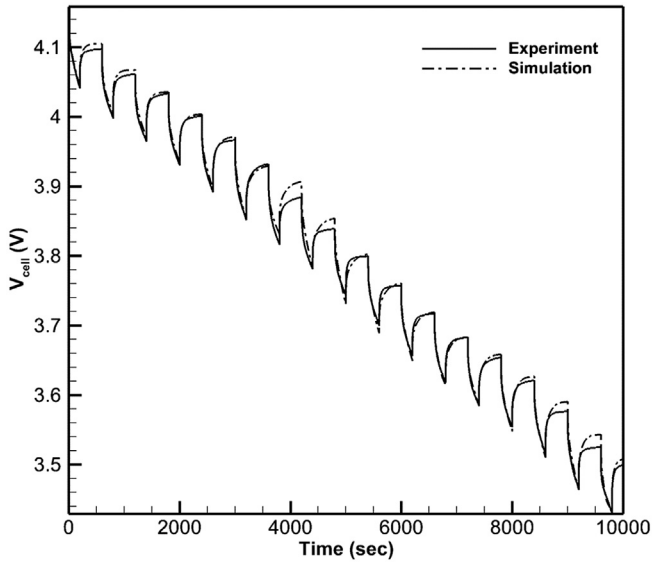


Fig. 3. Extraction of ECM parameters from iterative comparison of simulation and experiment data (discharge and rest test @25 °C).

Finally,  $y = R_1(T, \text{soc})$  is found out by plugging Eqs. (3) and (4) into Eq. (5).

$$y = R_1(T, \text{soc}) = (1-p) \cdot (1-q) \cdot y_{11} + p \cdot (1-q) \cdot y_{12} + (1-p) \cdot q \cdot y_{21} + p \cdot q \cdot y_{22} \quad (5)$$

By applying the above bilinear interpolation method, two-dimensional ECM parameters extracted from the experimental data of the actual Li-ion cell for the present study is shown in Fig. 4. Various different cell models can be also constructed with the same manner.

## 2.2. Multi-dimensional ECM

A schematic of calculation domains in the present multi-D lithium-ion cell model is presented in Fig. 5. The lithium-ion cell model has three domains (cell body, positive tab, negative tab). ECM presented above is inserted into each mesh of the cell body domain after scaling down according to mesh size. In order to incorporate all of small ECMs together, the following electric potential equations are solved in the cell body domain.

$$\left. \begin{aligned} \sigma_p \nabla^2 \Phi_p &= J \\ \sigma_n \nabla^2 \Phi_n &= -J \end{aligned} \right\} \text{where } J = J_{\text{rxn}} - J_s \quad (6)$$

In Eq. (6)  $J_{\text{rxn}}$  is volumetric electrochemical reaction current density whereas  $J_s$  is volumetric side-reaction current density defined as follows:

**Table 1**  
Two-dimensional data table for bilinear interpolation of ECM parameters for the present model.

T	SOC					
	0%	20%	40%	60%	80%	100%
−7 °C	R(1,1)	R(1,2)	—	—		
0 °C	R(2,1)	—				
25 °C	—					
45 °C	—					
R(4,6)						

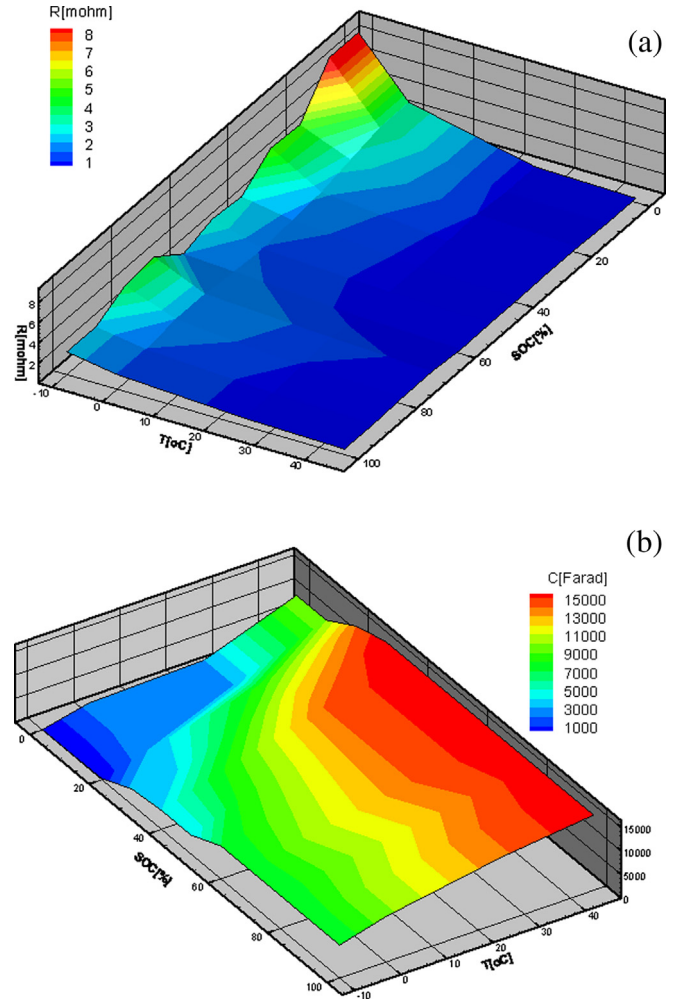


Fig. 4. ECM parameters acquired from bilinear interpolation for the present study: (a)  $R_1 = f(\text{SOC}, T)$ , (b)  $C_1 = f(\text{SOC}, T)$ .

$$J_s = J_s^{\text{ref}} \cdot e^{\left( \frac{-E_s}{R} \left( \frac{1}{T} - \frac{1}{T_{\text{ref}}} \right) \right)} \quad (7)$$

Side-reaction current,  $J_s$  adversely affects cell performance by generating mixed potential in the present model. It is added to the model in order to consider cell life degradation. Although an actual lithium-ion cell body is a composite structure made of several layers such as electrodes, separator and current collector, it is assumed that the dominant electrical current flow occurs in the in-plane direction along current collector which has the lowest electric resistance in the present model. Therefore, the average electric conductivity of the cell body domain in Eq. (6) is acquired by scale factors as follows:

$$\begin{aligned} \sigma_p &= \alpha_p \cdot \sigma_{\text{Al}} \quad \text{where } \alpha_p = \frac{n_{\text{Al-foil}} \cdot H_{\text{Al-foil}}}{H_{\text{cell}}} \\ \sigma_n &= \alpha_n \cdot \sigma_{\text{Cu}} \quad \text{where } \alpha_n = \frac{n_{\text{Cu-foil}} \cdot H_{\text{Cu-foil}}}{H_{\text{cell}}} \end{aligned} \quad (8)$$

This is because the present multi-D model is based on ECM, and it is not necessary to consider the detailed structure of each cell layer. In the positive tab which is made of aluminum, the following electric equation is solved.

$$\sigma_{\text{Al}} \nabla^2 \Phi_p = 0 \quad (9)$$

In the same manner, the negative tab equation is

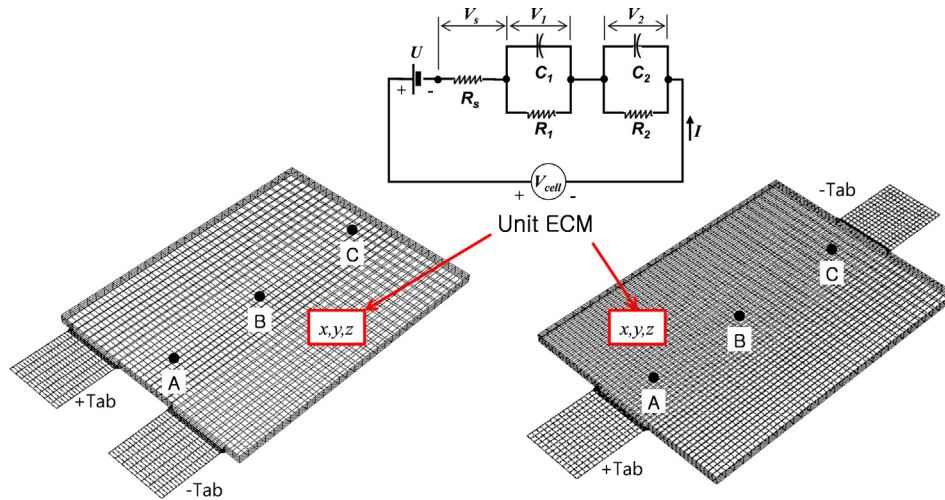


Fig. 5. Schematic of multi-D lithium-ion cell model which has constituting ECMs in each mesh node: (left) uni-directional cell, (right) bi-directional cell.

Table 2

Specification of the lithium-ion cell model for the present study.

Parameter	Sym.	Value	Unit
Cell length	$L_{\text{cell}}$	190	mm
Cell width	$W_{\text{cell}}$	142	mm
Cell thickness	$H_{\text{cell}}$	5.5	mm
Thickness of negative current collector	$H_{\text{Cu}}$	20	$\mu\text{m}$
Thickness of positive current collector	$H_{\text{Al}}$	20	$\mu\text{m}$
Thickness of negative electrode	$H_{\text{+}}$	50	$\mu\text{m}$
Thickness of positive electrode	$H_{\text{-}}$	55	$\mu\text{m}$
Thickness of separator	$H_{\text{sep}}$	20	$\mu\text{m}$
Lead-tab length	$L_{\text{tab}}$	40	mm
Lead-tab width	$W_{\text{tab}}$	40	mm
Lead-tab thickness	$H_{\text{tab}}$	0.2	mm
Nominal capacity (1C capacity)	$\bar{c}a\rho_0$	15.0	Ah
Cutoff voltage (max)	$V_{\text{max}}$	4.15	V
Cutoff voltage (min)	$V_{\text{min}}$	3.0	V
Density of cell	$\rho$	2400	$\text{kg m}^{-3}$
Specific heat of cell	$c_p$	1015	$\text{J kg}^{-1} \text{K}^{-1}$

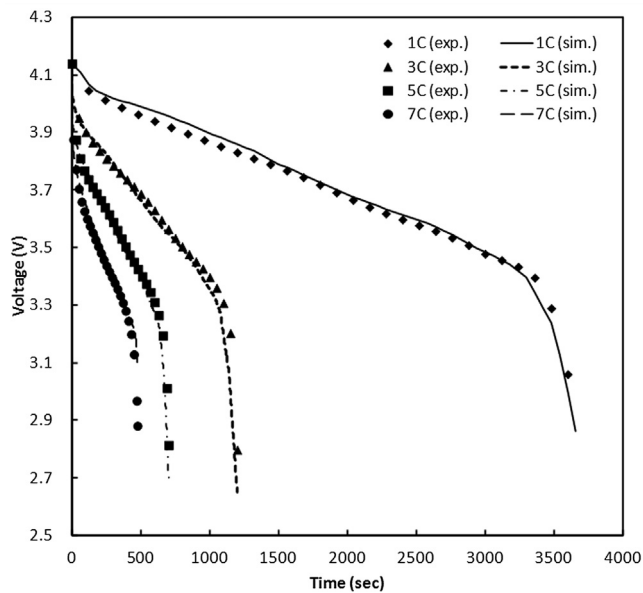


Fig. 6. Experimental validation of the multi-D model according to continuous discharging.

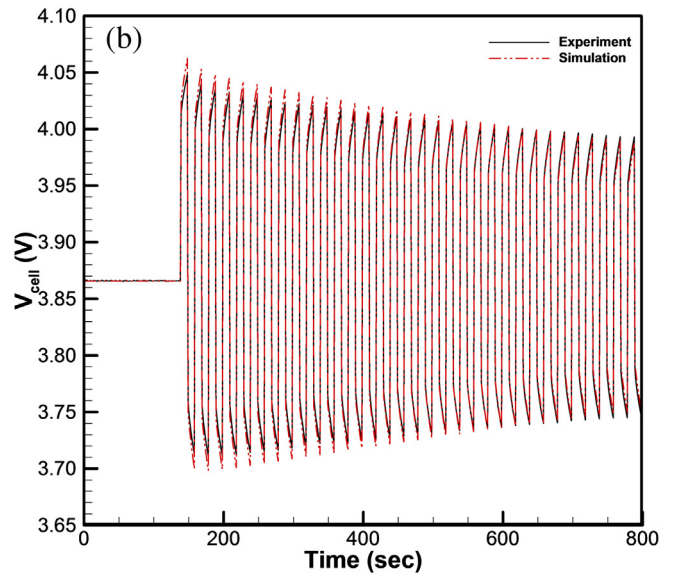
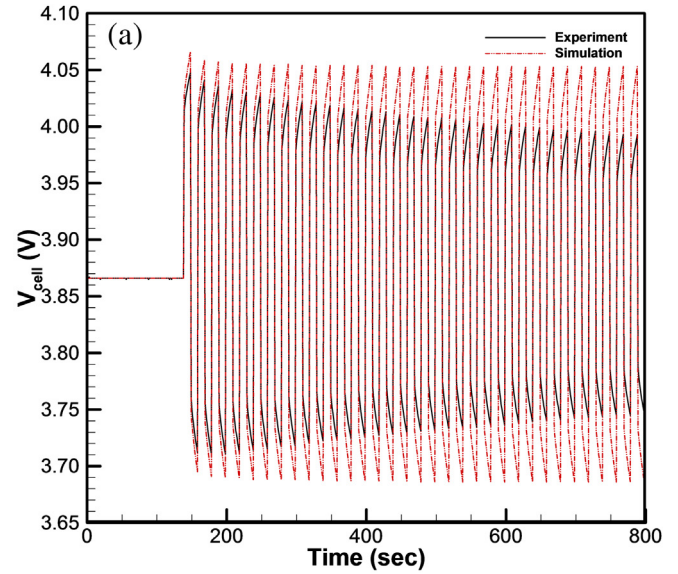


Fig. 7. Comparison of cell voltage profile between simulation and experiment under repetitive 80 A charging/discharging current pulse ( $\text{SOC}_{\text{init}} = 60\%$ ): (a) Isothermal model, (b) non-isothermal model.



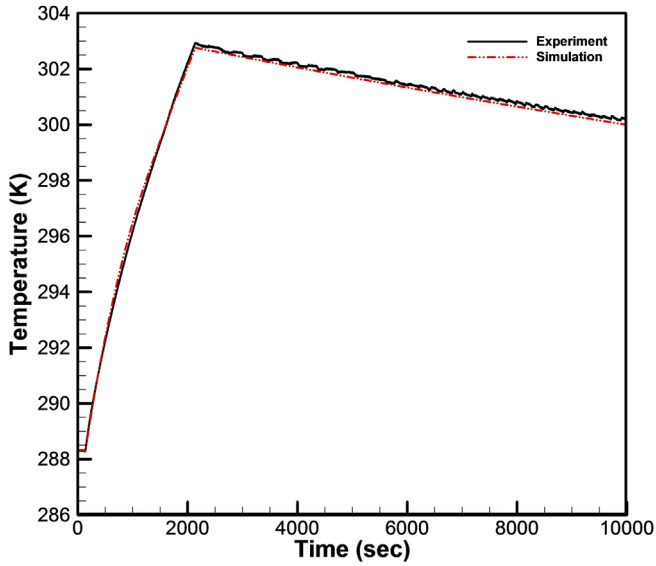


Fig. 8. Comparison of cell temperature (point B) between simulation and experiment under repetitive 80 A charging/discharging current pulse ( $T_{\text{amb}} = 288$  K,  $h = 0.18$  W m $^{-2}$  K $^{-1}$ ).

Table 3

Experimental validation summary (US06 driving test).

$T$ (°C)	Discharging & rest		US06 (5 cycles)	
	Avg. error (%)	Std. deviation (%)	Avg. error (%)	Std. deviation (%)
45	0.4	0.4	0.4	0.4
25	0.5	0.4	0.7	0.5
15	—	—	1.5	1.1
5	—	—	2.4	1.9
−10	1.2	0.8	2.9	1.8

$$\sigma_{\text{Cu}} \nabla^2 \phi_n = 0 \quad (10)$$

Note the above electrical equations came from the Maxwell equation by ignoring magnetic field effects. In the cell body domain where electrochemical reaction occurs ( $j \neq 0$ ), local cell voltage,  $V_{\text{cell}}(x, y, z)$  from ECM Eq. (1) is same as the potential difference calculated from Eq. (6) as follows:

$$\begin{aligned} V_{\text{cell}}(x, y, z) &= U(x, y, z) - V_s(x, y, z) - V_1(x, y, z) - V_2(x, y, z) \\ &= \phi_p(x, y, z) - \phi_n(x, y, z) \end{aligned} \quad (11)$$

From Eq. (11),  $V_s$  can be defined as follows:

$$V_s = U - \{\phi_p - \phi_n\} - V_1 - V_2 \quad (12)$$

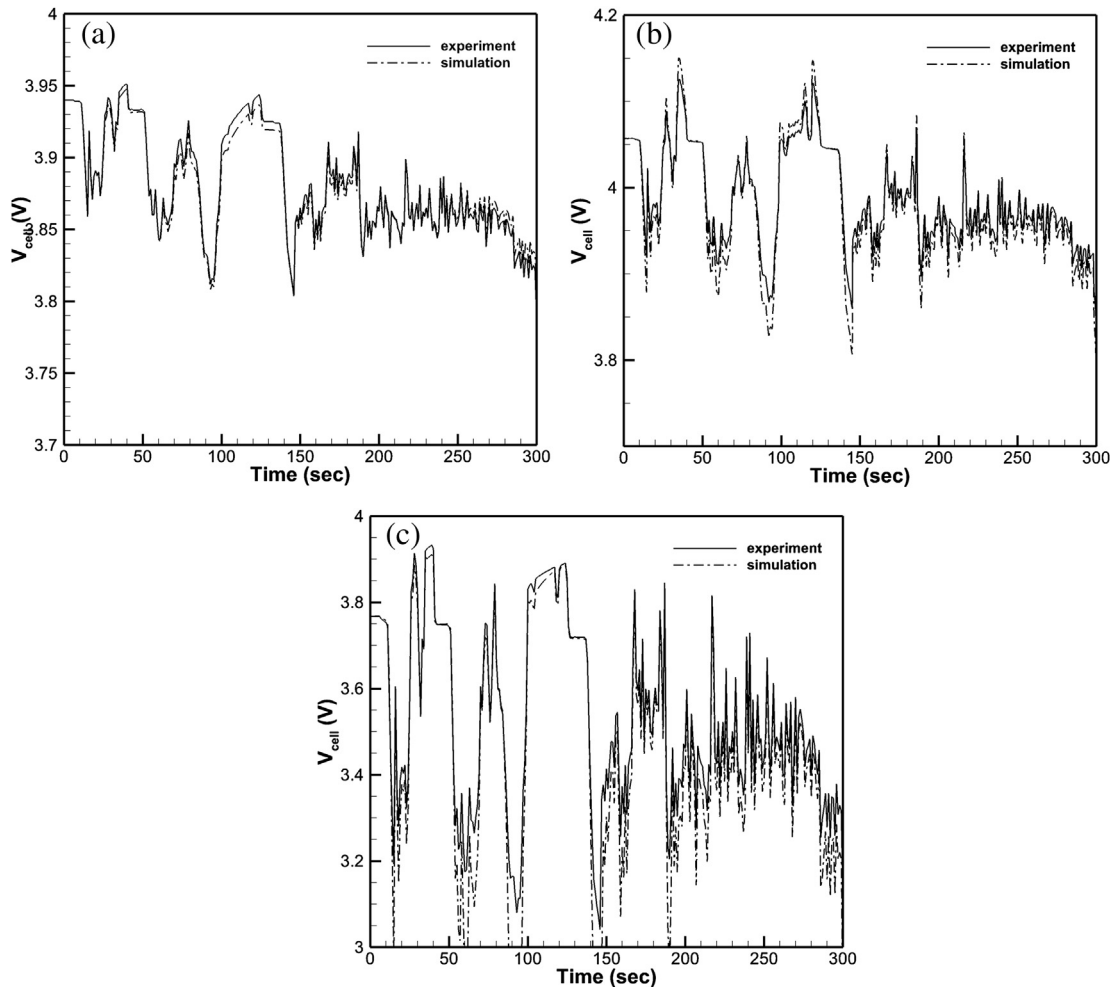
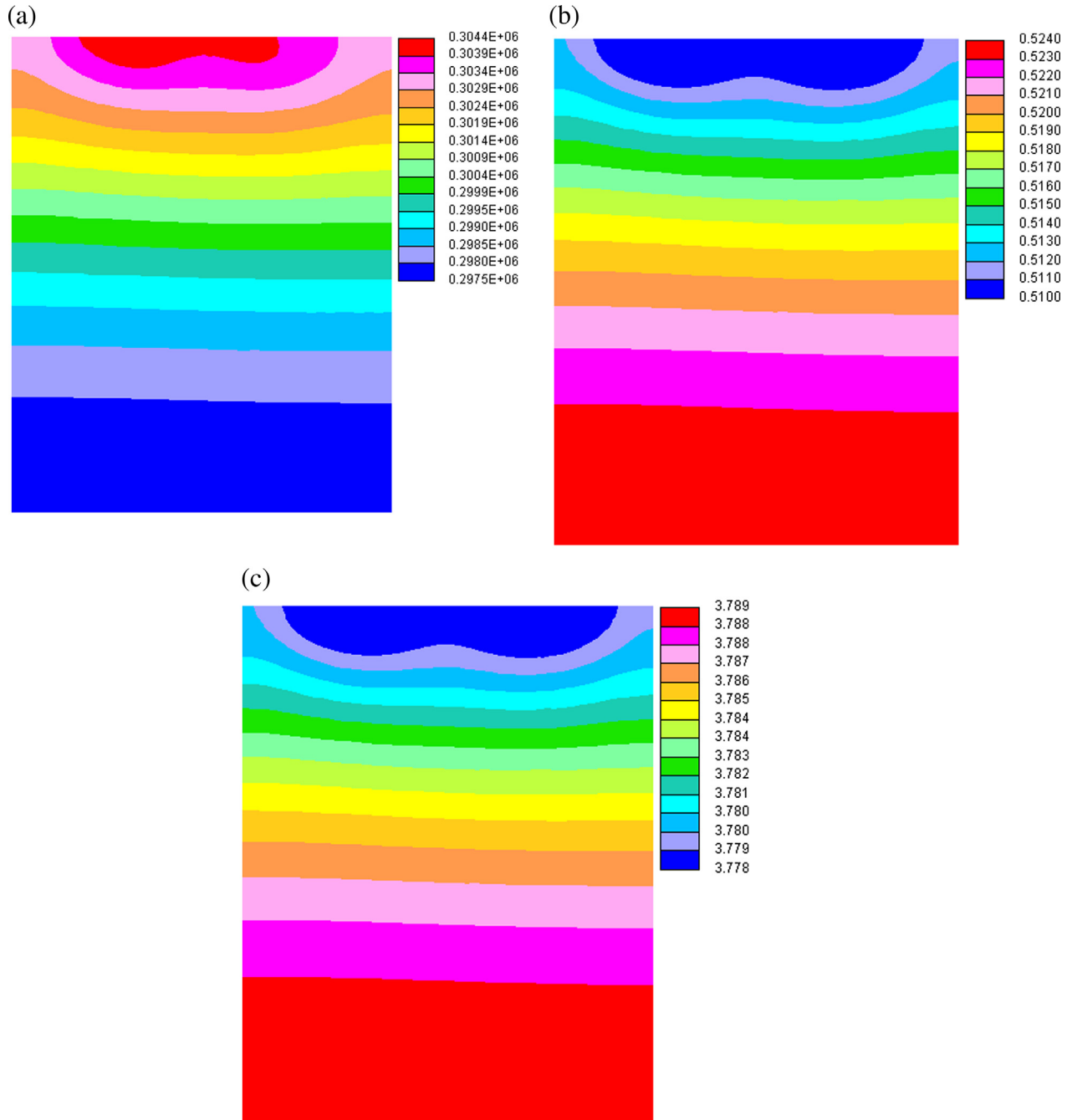


Fig. 9. Experimental validation of the present multi-D model: (a) US06 driving test @25 °C, (b) US06 driving test @15 °C, (c) US06 driving test @−10 °C.



**Fig. 10.** Distribution contour of (a) volumetric current density distribution (unit:  $\text{A m}^{-3}$ ), (b) SOC, and (c) OCV under 3C rate discharging condition @600 s.

Therefore, volumetric current density at point  $(x,y,z)$  can be found from Eq. (2) as

$$J_{\text{rxn}} = \frac{V_s}{V_{\text{cell}} \cdot R_s} \quad (13)$$

As the ECM parameters are strongly affected by temperature, it is necessary to couple the energy equation as follows:

$$\rho c_p \frac{\partial T}{\partial t} = \nabla(k \nabla T) - h(T - T_\infty) + \dot{q}'''$$

where  $\dot{q}''' = \dot{q}_{\text{rxn}}''' + \dot{q}_{\text{ohm}}''' = J(U - V + T \frac{dU}{dT}) + \iiint (\sigma \nabla \Phi)^2$  (14)

In the above energy equation, thermal conductivity of the cell body is acquired from

$$k_{\text{in-plane}} = \frac{1}{L_{\text{tot}}} \sum_i k_i L_i = 30 (\text{W m}^{-1} \text{ K}^{-1})$$

$$k_{\text{thru-plane}} = \left( \frac{1}{L_{\text{tot}}} \sum_i \frac{k_i}{L_i} \right)^{-1} = 0.8 (\text{W m}^{-1} \text{ K}^{-1}) \quad (15)$$

It is noteworthy that heat conduction occurs faster in the in-plane direction than in the thru-plane direction. The reaction term  $\dot{q}'''$  in Eq. (14) becomes zero in the positive tab and negative tab domain.

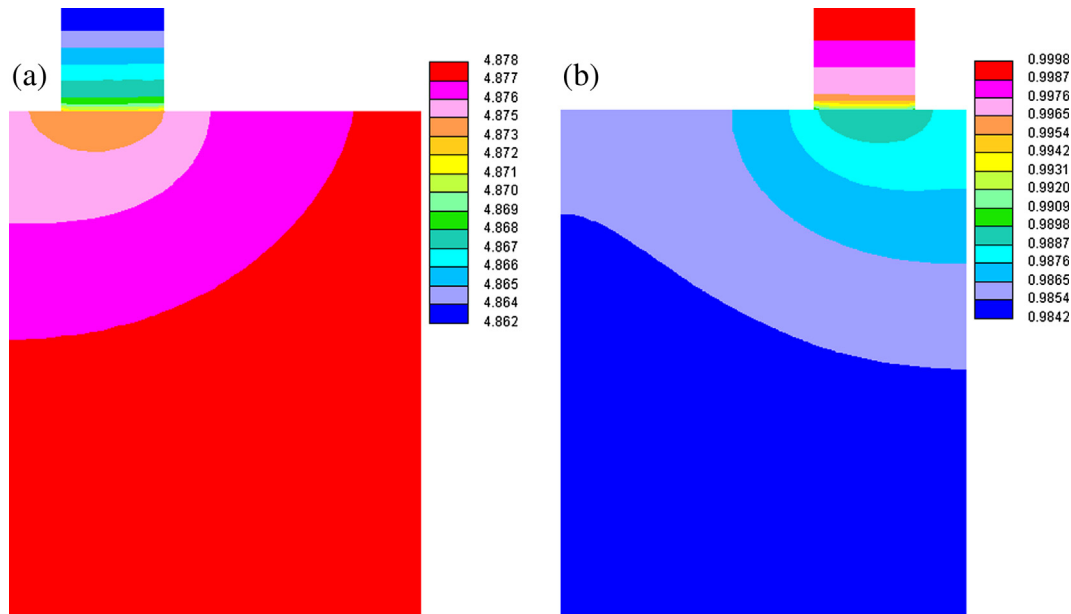


Fig. 11. Contour of positive and negative potential distribution (3C discharging) at 100 s (unit: V): (a) Positive potential, (b) Negative potential.

Boundary conditions for galvanostatic operation is given as follows:

$$-\sigma_{Cu}^{eff} \frac{\partial \phi_s}{\partial x} \Big|_{Cu-tab} = \sigma_{Al}^{eff} \frac{\partial \phi_s}{\partial x} \Big|_{Al-tab} = \frac{I}{A_{tab}} \tag{16}$$

The present model can also simulate other cell operation modes such as potentiostatic, power-driven, and pulse mode by changing boundary conditions above.

2.3. Degradation model

Battery degradation is expressed as capacity fade and impedance growth. Degradation can be caused when charging and

Table 4  
Degradation simulation cases.

Case no.	Run mode	C-rate	T (°C)	k (W m <sup>-1</sup> K <sup>-1</sup> )	Tab position	Remark
1	100 cycles	3	25	30.0	Uni-directional	Baseline case
2	100 cycles	5	25	30.0	Uni-directional	Effect of C-rate
3	100 cycles	3	45	30.0	Uni-directional	Effect of temperature
4	100 cycles	3	25	5.0	Uni-directional	Effect of thermal conductivity
5	100 cycles	3	25	30.0	Bi-directional	Effect of lead-tab position

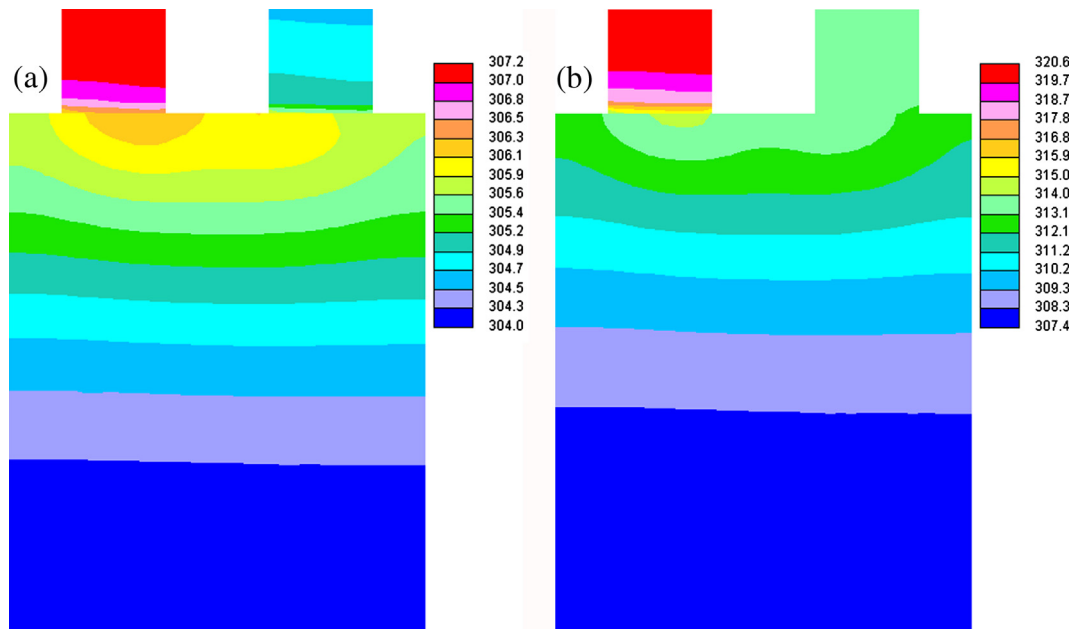


Fig. 12. Contour of cell temperature distribution (unit: K): (a) 3C rate @600 s, (b) 5C rate @300 s.

discharging of a battery is repetitively cycled, which is called cycle-life loss. When a battery is stored in a place for long time without operation, degradation may also occur, which is called calendar-life loss. Usually, both degradation modes take place in a combined manner during the entire life time of battery. In order to develop long-lasting batteries, it is important to understand the cause and mechanism of battery degradation. Degradation originates from several causes as lithium-ion battery is a very complicated system [12]. It is still unclear how causes of degradation are related and how they affect the cell life. Therefore, it is not easy to construct a physics-based degradation model although several studies have been conducted under restricted conditions [13–17]. Empirical models [10] can be constructed relatively easily although it is not easy to collect experimental data for long period. Semi-empirical models [11] can be applied to more general simulation cases than empirical models because model parameters are flexible.

Recently, the sizes of lithium-ion cells have become larger. In this case, local degradation distribution becomes more important, which may come from cell size, shape or lead-tab position. As most of degradation model listed above are 1-D or lumped-scale model, they cannot predict local degradation coming from dimensional effect. Multi-D cell model has capability of predicting local degradation distribution. Various empirical or semi-empirical degradation models can be incorporated with the present multi-D model. In this paper, a simple empirical degradation model which predicts capacity fade and resistance growth according to cell operation and exposure to temperature is presented to show local degradation distribution.

The present model assumes nominal capacity at location  $(x, y, z)$  is a function of total accumulated coulomb ( $Q$ ) as proposed by Bloom et al. [10].

$$\bar{cap} = \bar{cap}_0 (1 - \alpha \cdot Q^{1/2}) \quad (17)$$

Eq. (17) imitates cell capacity fade by available lithium loss. Local SOC is determined based on the updated nominal capacity in Eq. 2(17).

$$soc = soc_0 - \frac{1}{\bar{cap}} \cdot \int_{\text{time}} J(t) \cdot dt \quad (18)$$

Accumulated coulomb is sum of reaction current ( $J_{rxn}$ ) and side-reaction current ( $J_s$ ). Side reaction current is added to consider calendar life.

$$Q(t) = \int_t (J_{rxn} + J_s) dt \quad (19)$$

State of health is defined as

$$soh = \frac{\bar{cap}}{\bar{cap}_0} \quad (20)$$

Three resistance terms are modified as a function of SOH to consider resistance growth.

$$\begin{aligned} R_s &= R_{s,0} \{1 + \beta_s \cdot (1 - soh)\} \\ R_1 &= R_{1,0} \{1 + \beta_1 \cdot (1 - soh)\} \\ R_2 &= R_{2,0} \{1 + \beta_2 \cdot (1 - soh)\} \end{aligned} \quad (21)$$

In Eq. (21),  $\beta$  is adjustable fitting parameter. Because the present model solves governing equation at each time step with given boundary condition, the model can simulate cell degradation under various operating conditions under any current (or power) load profile and thermal profile. Although relatively simple degradation model for multi-D application is introduced in this study, more

sophisticated life models [18] can be implemented into the present multi-D model.

### 3. Result and analysis

Specification of a 15 Ah-class Li-ion cell used for the present study is presented in Table 2. The lithium-ion cell has a positive electrode made of layered NMC (Lithium nickel manganese cobalt) and manganese spinel while graphite and carbon are blended to construct a negative electrode. The multi-D model is solved by finite volume method (FVM). Solution is assumed to converge when residuals reaches  $10^{-9}$ .

#### 3.1. Baseline multi-dimensional cell model

Experimental validation of the present multi-D model under several C-rate discharging conditions is presented in Fig. 6. The model shows pretty good accuracy up to 7C discharging condition. However, simulation result starts to deviate from the experimental data above 7C-rate. This is because it is difficult to handle mass transport limiting phenomena with standard ECM. Additional variables such as Warburg circuit will be helpful to resolve this problem, which is not covered in this study.

In order to validate dynamic voltage response of the model against experimental data, a repetitive charging/discharging current pulse test during 2000 s is conducted as shown in Fig. 7(a). When temperature is maintained constant, simulation result shows almost same magnitude of voltage response since same amount of coulomb is charged and discharged during the test. However, the actual cell shows slightly diminishing magnitude of voltage response. This is because the cell resistance decreases as the cell temperature increases during the pulse test. Temperature profile during the pulse test is shown in Fig. 8. When the thermal model is applied to the test scenario, ECM parameters are updated according to the temperature and the voltage response of the model matches well with the experimental data as shown in Fig. 7 (b). Driving simulation according to US06 driving profile is conducted at temperature of 25 °C, 15 °C, and –10 °C (see Fig. 9). Note 15 °C and –10 °C were not included in Table 1, which means these two simulation cases are conducted with bi-linearly interpolated parameters. Although interpolated model parameters are used,

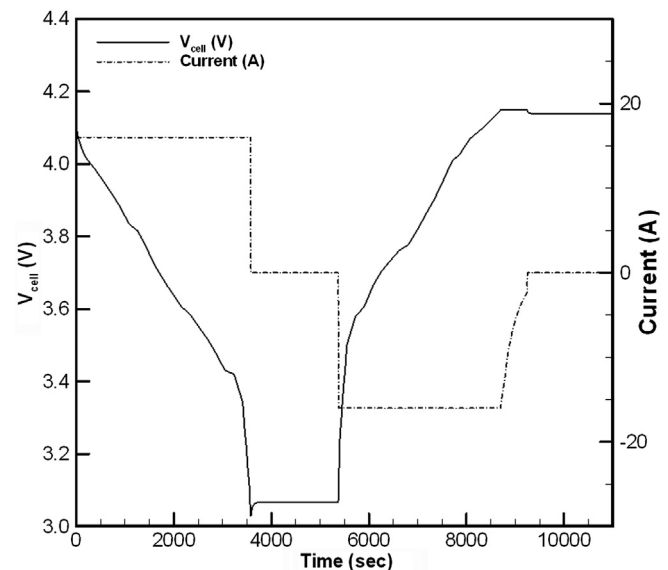


Fig. 13. Simulated voltage profile of the cell for the first cycle (case #1).



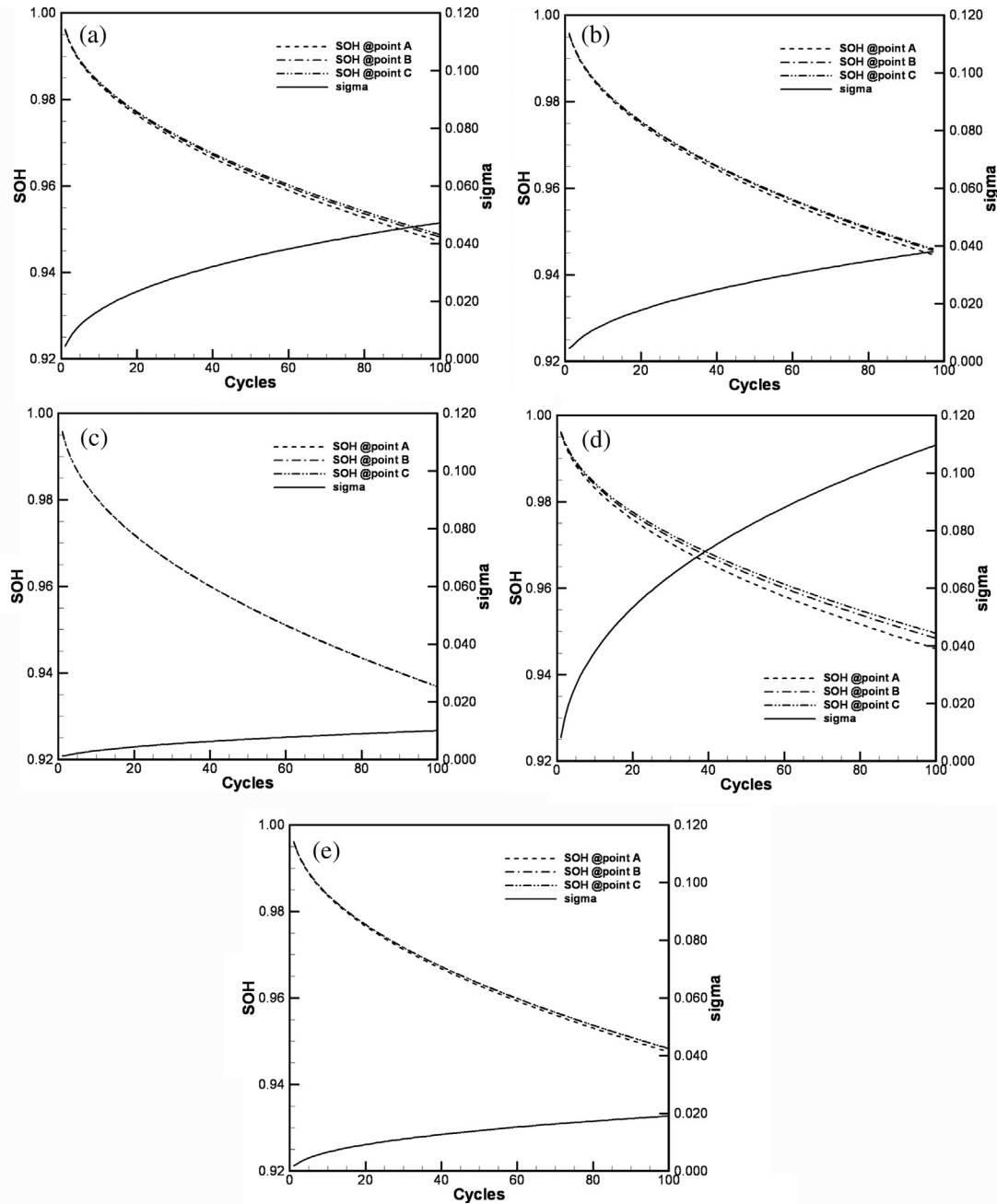


Fig. 14. SOH according to cyclic operation mode of the multi-D model: (a) case #1, (b) case #2, (c) case #3, (d) case #4, (e) case #5.

simulation result agrees well with experiment data. Experimental validation under other conditions is summarized in Table 3. Model accuracy slightly decreases when the cell operates at low temperature. This is because model parameters become more sensitive to the ambient temperature under low temperature conditions. In addition, it is difficult to get accurate model parameters at low temperature because maintaining isothermal condition of the operating cell is not easy.

Volumetric current density (reaction rate) during 3C rate discharging condition is presented in Fig. 10(a). It is observed that current density is strongest near lead-tab because electric current produced in the electrode is collected by lead-tab. As the current density is high near lead-tab region, local SOC is low there also as shown in Fig. 10(b). Local OCV can be found according to local SOC

(Fig. 10(c)). OCV near lead-tab drops faster than other region since reaction rate is high there during discharging. These results agree with our previous intuitive expectations. Potential field distribution in each electrode is shown in Fig. 11. Potential field distribution is strongly affected by the effective electric conductivity in Eq. (8). When the current collector is thick and made of more conductive material, the effective electric conductivity becomes high. As a result, it improves the uniformity of potential, OCV, and SOC distribution in each electrode, which results in reduced voltage loss. Amount of local heat generation in the cell is calculated from Eq. (14) with the current density and potential distribution that are calculated. Then, temperature distribution is obtained by solving energy equation. As the present cell model is thermally coupled, local temperature is used to find appropriate temperature-dependent model

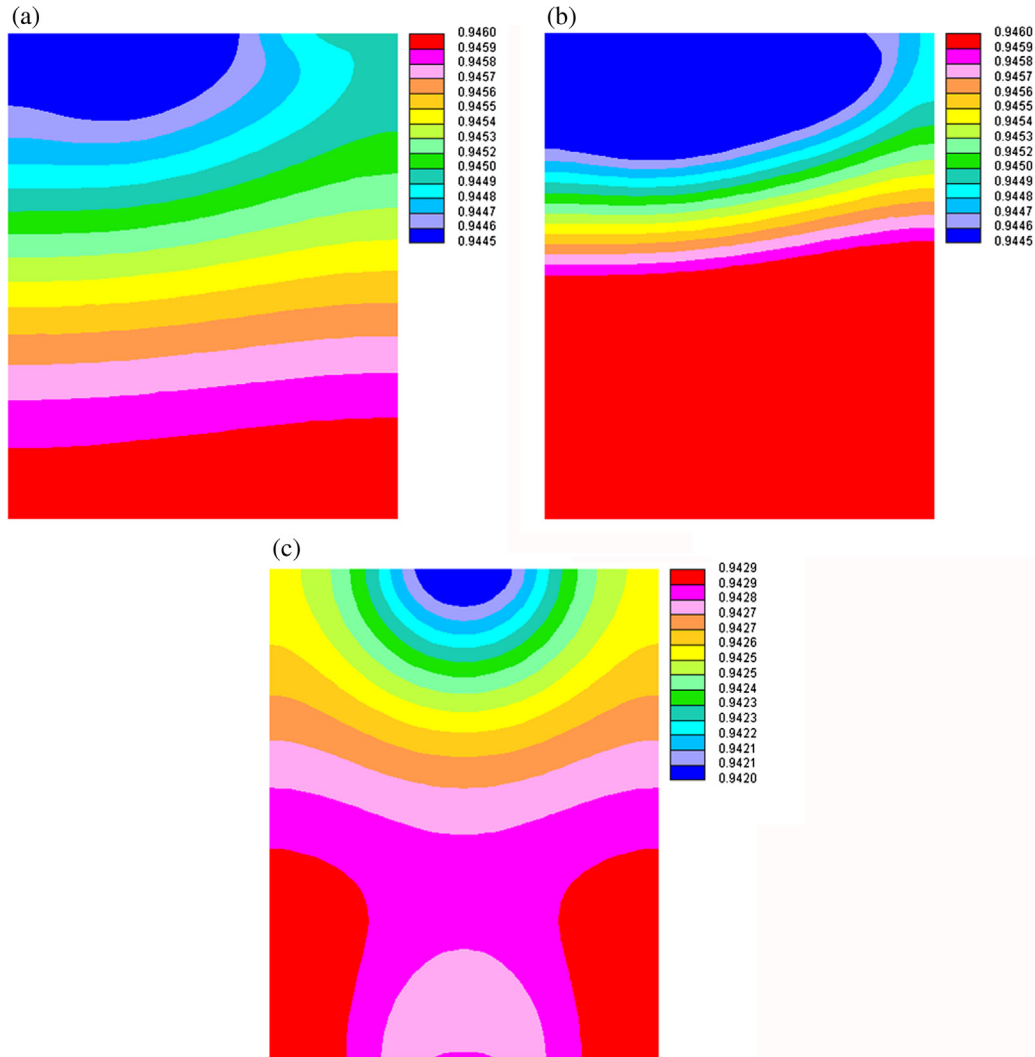


Fig. 15. Contours of SOH during cyclic degradation test (after 100 cycles): (a) case #1, (b) case #4, (c) case #5.

parameters such as resistances. Fig. 12 shows temperature distribution of the cell. As the electric current converges to lead-tab, temperature is highest near lead-tab region. Temperature distribution in the cell body domain is strongly affected by thermal conductivity. If thermal conductivity is too low, temperature difference in a cell becomes large and it may deteriorate state of health in a cell.

### 3.2. Degradation effect

In this part, the effect of degradation on SOH of a cell is discussed with the degradation model. Table 4 lists simulation cases conducted to examine degradation effect on the cell performance according to C-rate, temperature, thermal conductivity, and lead-tab position.

In order to conduct a cyclic degradation simulation, a single cycle with the baseline cell model is prepared as shown in Fig. 13. First, the cell discharges until the cell voltage reaches lower cutoff voltage. After taking rest for 0.5 h, the cell is charged until the cell voltage reaches upper cutoff voltage. Finally, the cell is charged with constant voltage until charging current reaches 5% of 1C current. This run is cycled 100 times to examine the degradation of the cell.

Average SOH of the baseline cell according to cycle number is presented in Fig. 14(a)–(c). It is observed that SOH decreases faster when the cell operates under severe operating condition such as high C-rate and high temperature. However, calculation result shows that standard deviation (sigma) of SOH is low under severe operating condition. In other words, uniformity of SOH becomes improved. When the cell operates under severe condition, cell temperature is elevated and the cell resistances are reduced according to high temperature. As the cell resistances are reduced, uniformity of local overpotential in the cell is improved resulting in uniform accumulated coulomb i.e. state of health. This result happens since the present model parameters are strongly affected by temperature. If thermal conductivity of a cell is low, temperature uniformity will be worsened which leads to low SOH uniformity as shown in Fig. 14(d). This result implies high thermal conductivity of a cell mitigates local degradation due to improved uniformity of temperature distribution. Calculation result revealed that the cell with bi-directional lead-tabs shows the best degradation performance (the highest remaining SOH and the highest SOH uniformity) compared to other cases. Local distribution contour of SOH is shown in Fig. 15. SOH in the region near lead-tab is lower than other region since the region near lead-tab experienced relatively severe operation (high current density and high temperature) compared

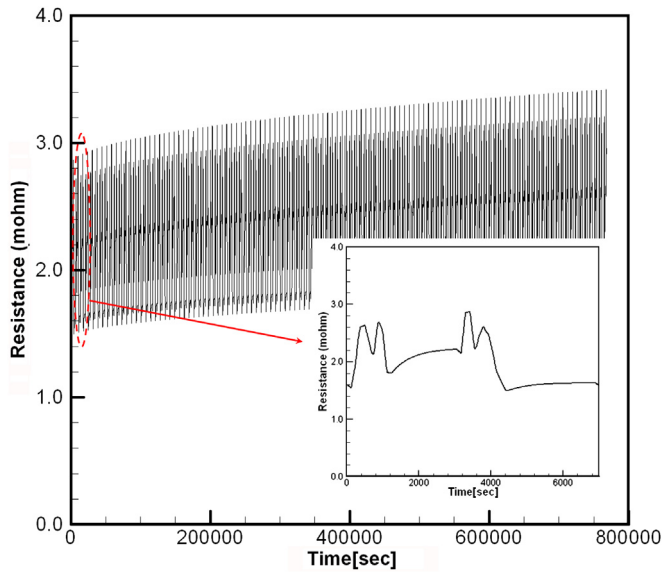


Fig. 16. Cell resistance ( $R_2$ ) variation according to cyclic operation case #1 (small graph shows cell resistance variation in a single cycle: discharging/rest/charging/rest).

to the other regions. This local degradation will be mitigated if lead-tab is wide and thick, which may lower heat generation and current density near lead-tab. The cell with bi-directional lead-tabs shows better distribution of temperature and SOH than the cell with uni-directional lead-tabs does. In the cell with bi-directional lead-tabs, temperature near positive lead-tab had been maintained relatively higher than other regions, which results in low SOH there (see Fig. 15(c)).

Cell resistances increase as the cell degradation goes on. Fig. 16 shows variation of a cell-averaged ECM resistance when the cell operates for 100 cycles. Magnified figure in the plot shows resistance variation in a single cycle. Note resistance difference between SOC 0% and SOC 100% in a cycle increases as the cell degradation goes. As the cell resistance increases, overpotential ( $U-V$ ) increases

and the amount of heat generation increases also according to Eq. (14). This leads to temperature increase as SOH of the cell is worsen as shown in Fig. 17. Therefore, it is important to consider temperature increase due to cell degradation when designing battery pack cooling system.

#### 4. Conclusion

A multi-D model of lithium-ion cell has been developed. The model is based on ECM and it is capable of simulating various cell operation modes with good accuracy. In order to consider effect of temperature and SOC on the cell performance, model parameters were bilinearly interpolated. Simulation results show good agreement with experiment data under various operation conditions. Local degradation effects have been elucidated by applying an empirical degradation model to the present multi-D model. Degradation became worsen under severe condition such as high storage temperature and high C-rate. It was observed that low thermal conductivity of a cell is harmful to uniformity of cell SOH. Local distributions of potential, SOC, SOH have been examined, which is difficult to observe with conventional experimental methods.

The present model has potential to be extended to various applications. For example, by separating positive and negative electrode, the present multi-D model can be extended to study battery safety such as external shorts or nail-penetration. In addition, the developed model can be extended to transient CFD analysis of large-scale battery pack, which is necessary for designing battery pack cooling system.

Through an extensive work of model validation, it was confirmed that the present multi-D model works well with single-phase active materials such as NMC (Lithium nickel manganese cobalt), LCO (Lithium cobalt oxide), LMO (Lithium manganese spinel), and graphite. But, ECM sub-model inserted into the present multi-D model needs to be modified if the electrode is blended with phase-changing materials such as  $\text{LiFePO}_4$ , and LTO (Lithium titanate oxide) in order to reflect phase-transition phenomena.

#### List of symbols

$A$	area ( $\text{cm}^2$ )
$c_p$	specific heat ( $\text{J kg}^{-1} \text{K}^{-1}$ )
$C$	capacitance (Farad)
$cap$	capacity (Ah)
$E_a$	activation energy ( $\text{J mol}^{-1}$ )
$F$	Faraday constant ( $96487 \text{ C mol}^{-1}$ )
$h$	heat transfer coefficient ( $\text{W m}^{-2} \text{K}^{-1}$ )
$H$	thickness (cm)
$I$	current (A)
$J$	volumetric current density ( $\text{A cm}^{-3}$ )
$k$	thermal conductivity ( $\text{W m}^{-1} \text{K}^{-1}$ )
$L$	length (cm)
$m$	mass (kg)
$n$	number
$R$	resistance (ohm), universal gas constant ( $8.314 \text{ J mol}^{-1} \text{K}^{-1}$ )
soc	state of charge
soh	state of health
$t$	time (sec)
$T$	temperature (K)
$V$	voltage ( $\text{V}$ )
$w$	width (cm)
$U$	open circuit potential (V)
$\dot{q}$	heat source (W)
$Q$	charge (Coulomb)

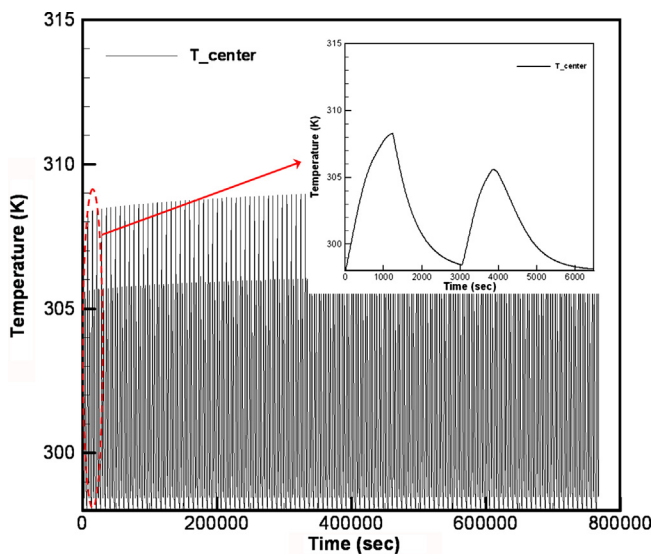


Fig. 17. Temperature at the center of the cell during cyclic operation case 1 (small graph shows temperature variation in a single cycle: discharging/rest/charging/rest).

$V$  voltage (V)  
 $V$  volume ( $\text{m}^3$ )

#### Greek

$\alpha$  data fitting coefficient  
 $\eta$  overpotential (V)  
 $\rho$  density ( $\text{kg m}^{-3}$ )  
 $\sigma$  electric conductivity ( $\text{S cm}^{-1}$ )  
 $\Phi$  potential (V)

#### Superscripts and subscripts

0 initial  
 amb ambient  
 cell cell  
 eff effective  
 $n$  negative  
 $p$  positive  
 ref reference  
 rxn reaction  
 $s$  serial, side reaction  
 sep separator  
 tab lead-tab

#### References

- [1] M. Doyle, T.F. Fuller, J. Newman, J. Electrochem. Soc. 140 (1993) 1526.
- [2] T.F. Fuller, M. Doyle, J. Newman, J. Electrochem. Soc. 141 (1994) 1.
- [3] R. Darling, J. Newman, J. Electrochem. Soc. 144 (1997) 4201.
- [4] M.W. Verburgge, R.S. Conell, J. Electrochem. Soc. 149 (1) (2002) A45.
- [5] B.Y. Liaw, G. Nagasubramanian, R.G. Jungst, D.H. Doughty, Solid State Ionics 175 (2004) 835.
- [6] M.W. Verburgge, P. Liu, J. Power Sources 174 (2007) 2.
- [7] M. Dubarry, B.Y. Liaw, J. Power Sources 174 (2007) 856.
- [8] K.H. Kwon, C.B. Shin, T.H. Kang, C.S. Kim, J. Power Sources 163 (2006) 151.
- [9] H. Gu, J. Electrochem. Soc. 130 (7) (1983) 1459.
- [10] I. Bloom, B.W. Cole, J.J. Sohn, S.A. Jones, E.G. Polzin, V.S. Battaglia, G.L. Henriken, C. Motloch, R. Richardson, T. Unkelhaeuser, D. Ingersoll, H.L. Case, J. Power Sources 101 (2001) 238.
- [11] R. Spotnitz, J. Power Sources 113 (2003) 72.
- [12] J. Vetter, P. Novak, M.R. Wagner, C. Veit, K.C. Moller, J.O. Besenhard, M. Winter, M. Wohlfahrt-Mehren, C. Vogler, A. Hammouche, J. Power Sources 147 (2005) 269.
- [13] P. Darling, J. Newman, J. Electrochem. Soc. 145 (3) (1998) 990.
- [14] P. Arora, R.E. White, J. Electrochem. Soc. 145 (10) (1998) 3647.
- [15] P. Arora, M. Doyle, R.E. White, J. Electrochem. Soc. 146 (10) (1999) 3543.
- [16] P. Ramadass, B. Haran, P.M. Gomadam, R.E. White, B.N. Popov, J. Electrochem. Soc. 151 (2) (2004) A196.
- [17] G. Sikha, B.N. Popov, R.E. White, J. Electrochem. Soc. 151 (7) (2004) A1104.
- [18] Battery Calendar Life Estimator Manual Revision 1, Advanced Energy Storage Publications, Idaho National Laboratory, 2012.